Modeling of Input Nonlinearity and Waveform Engineered High Efficiency Class-F Power Amplifiers

Sagar K. Dhar, Tushar Sharma, *Student Member, IEEE,* Ning Zhu, Ramzi Darraji, *Member, IEEE,* Damon G. Holmes, *Senior Member, IEEE,* Joseph Staudinger, *Fellow, IEEE,* Mohammad Helaoui, *Senior Member, IEEE,* Vince Mallette, and Fadhel M. Ghannouchi, *Fellow, IEEE*

Abstract— **A comprehensive time-domain modeling and a generalized design methodology for input and output waveform engineered Class-F power amplifiers (PAs) are presented in this paper. A closed-form relationship between input nonlinearity and second harmonic source impedance (Z_{2S}) termination is presented from which efficiency and output power performance are predicted for Class-F PAs. The maximum, minimum, and safe Z_{2S} design space for a Class-F PA are identified. Moreover, the derived design equations show that the typical fundamental load of a Class-F PA operation must be re-engineered in the presence of input nonlinearity in order to achieve optimum efficiency performance. The theoretical analyses are first validated with pulsed vector load-pull measurements (VLP) with a Gallium Nitride (GaN) 2 mm device. Then, high-power (210 W) GaN 24 mm devices with in-package Z_{2S} terminations are implemented. Measurement results with the new source and load design space show efficiency improvement of 4.4% compared to the nominal Class-F PA.**

***Index Terms*— class-F, harmonic tuning, input nonlinearity, multi-harmonic load-pull, power amplifier, pulsed load-pull, waveform engineering.**

I. Introduction

The quest for high-efficiency power amplifier (PA) design is long-run. To enhance the PA efficiency performance, typically, harmonic drain voltage and/or current are manipulated which are examined as early as in 1920s [1]. Since then the output load networks are explored extensively from the tuned load (TL- all load harmonics are short-circuited) to bi-harmonic, poly-harmonic or in general to harmonic tuned (HT) ones [2]. In the HT PAs [3]–[11], efficiency is improved by harmonic load terminations which minimizes the overlapping between voltage and current waveforms. Although specific load harmonic termination increases the design complexity of PA load networks, they significantly enhance the PA efficiency performance compared to the TL ones [12]. That being said, a PA load network with inappropriate harmonic terminations could severely affect PA performance [9], [13]. Apart from load, source harmonics also play a vital role in PA efficiency performance. As such, it is important to model and understand the impact of input-output harmonic tuning such that the appropriate design space can be identified to probe the optimum power device performance.

Traditionally, input second harmonic impedance (Z_{2S}) is avoided by considering a short circuit termination in high efficiency HT PA topology like Class-F considering the fact that a Z_{2S} termination other than short can be detrimental since it increases the conduction angle of the device [14]–[17]. However, it has been recently investigated that there are possible Z_{2S} terminations which can also reduce the device conduction angle [18]. The gate voltage and consequently the drain current waveforms are shaped by different Z_{2S} terminations, which result in device conduction angle and performance variation. The impact of input nonlinearity is investigated in single frequency or broadband applications [19]–[23], but a comprehensive modeling and performance analysis are still missing for Class-F PAs with input-output harmonic tuning. Moreover, an analytical model exploring the relationship between second harmonic source termination and input nonlinearity is long overdue.

Starting from an equivalent input nonlinear circuit, a closed-form relationship between input nonlinearity and source harmonic terminations is developed in this paper. Based on this model, new time-domain analyses of a Class-F PA are conducted based on which the minimum, maximum, and safe Z_{2S} design space are identified. The flow-chart predicting Class-F PA efficiency and output power performance with respect to Z_{2S} terminations is shown in Fig. 1. The load pull setup in Fig. 1 is utilized to validate the theoretical prediction of Class-F PA performance and the waveforms at different nodes of the devices. These analyses are significant in that it effectively predicts second harmonic source pull performance

This work was supported in part by the National Research Council of Canada and in part by Alberta Innovates Technology Futures.

S. K. Dhar, and F. M. Ghannouchi are with the University of Calgary, Calgary, AB T2N 1N4, Canada (e-mail: sagar.dhar@ucalgary.ca; fadhel.ghannouchi@ucalgary.ca).

T. Sharma, N. Zhu, D. G. Holmes, and J. Staudinger are with the NXP Semiconductors, Chandler, AZ 85224, USA (e-mail: tushar.sharma@nxp.com; ning.zhu@nxp.com; damon.holmes@nxp.com; joseph.staudinger@nxp.com)

R. Darraji is with the Ericsson Canada Inc. Ottawa, ON K2K 2V6, Canada (email: ramzi.darraji@ericsson.com)

V. Mallette is with the Focus Microwaves, Montreal, QC H9B 3H7, Canada (email: vince@focus-microwaves.com)

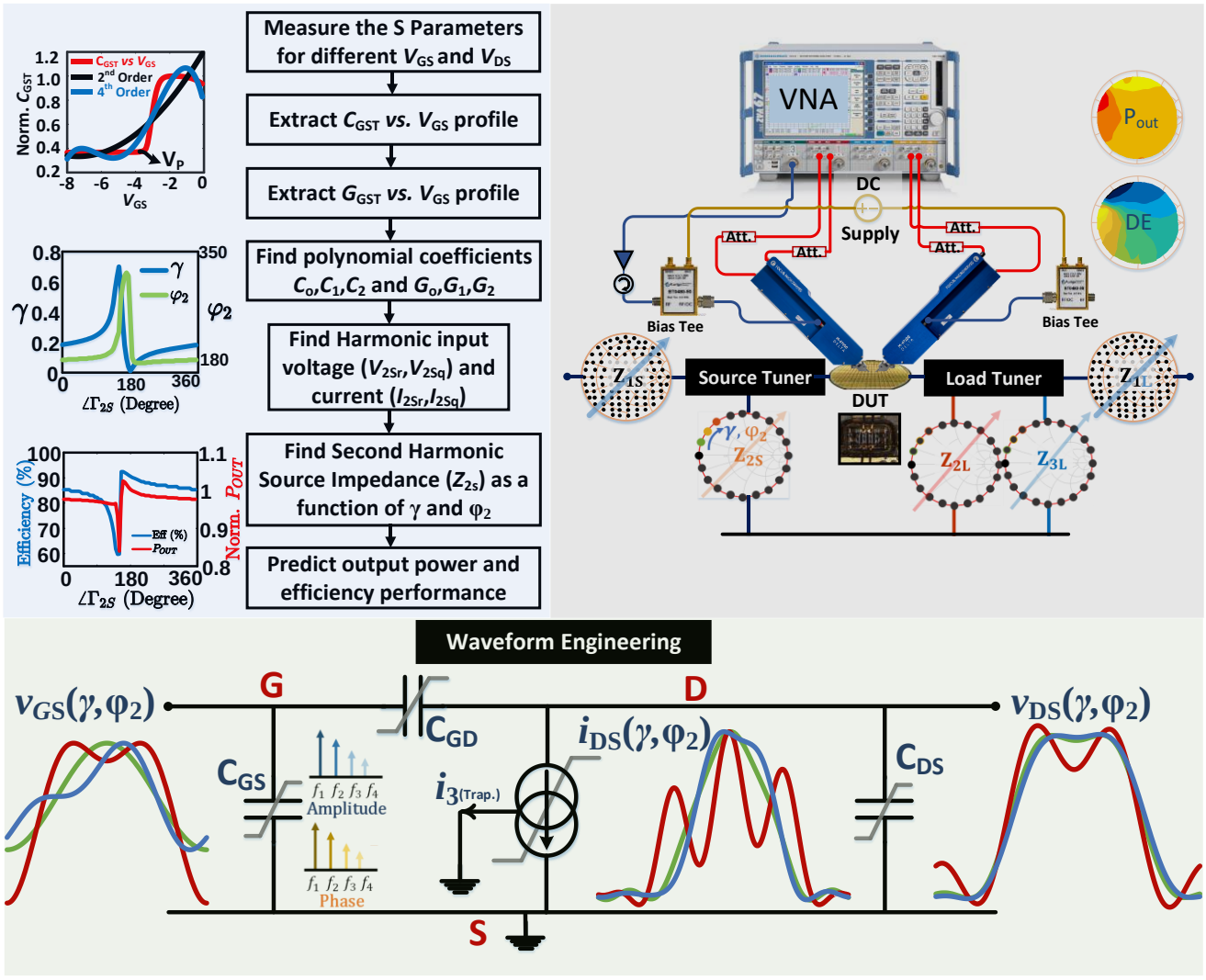

Fig. 1. Characterization, modeling, and functional block diagram of a Class F PA with input-output waveform engineering.

of a Class-F PA for the first time. It has been observed that the Class-F performance is greatly sensitive to the input nonlinearity unlike Class F^{-1} PA [21]. Besides, the analyses show that a distinct design strategy for Class-F HT PAs is required in the presence of input nonlinearities. We demonstrate that, due to the current waveform shaping by the input nonlinearity, the fundamental load termination must be readjusted in order to recover and maintain optimum Class-F PA performance. Thus, input nonlinearity is exploited to leverage the combined benefits of input-output harmonic manipulation and to develop a high-efficiency Class-F PA.

The rest of the paper is organized as follows. In Section II, the input nonlinearity is modeled in relation to second harmonic source terminations. The generalized theory of input-output harmonic tuned Class-F PA performance is presented in Section III. The practical validations of the theoretical analysis are discussed in Section IV.

II. Input Nonlinearity and Source Terminations

The input nonlinearity of an active device is a result of the nonlinear gate to source capacitance (C_{GS}) profile with respect to the gate voltage (v_{GS}). Such nonlinearity shapes the input voltage waveform depending on the source termination as depicted in Fig. 1 and impacts the PA performance significantly [18]. To analyze the nonlinear C_{GS} versus v_{GS} profile and its impact, a simplified input circuit is considered as shown in Fig. 2(a). The total input gate-source capacitance (C_{GST}) and conductance (G_{GST}) are defined by the Miller theorem [24] as

$$C_{GST} = C_{GS} + C_{GD}(1+A_v) \quad (1)$$

$$G_{GST} = G_{GS} + G_{GD}(1+A_v) \quad (2)$$

where C_{GD} and G_{GD} are the gate-drain capacitance and conductance, respectively, and $-A_v$ is the voltage gain of the device. Although G_{GST} is comparatively small, it is still considered for sake of completeness of the analysis. The nonlinear gate-source capacitance and conductance profile of a GaN device with gate-source voltage are shown in Fig. 2(b) and 2(c), respectively. It can be observed that the onset of C_{GST} and G_{GST} nonlinearity is due to v_{GS} swings higher than the device pinch-off voltage (V_P) when charge inversion mechanism starts over. This implies that the input nonlinearity is also triggered way before the saturation point of the PA and can influence both the small and large signal PA behavior.

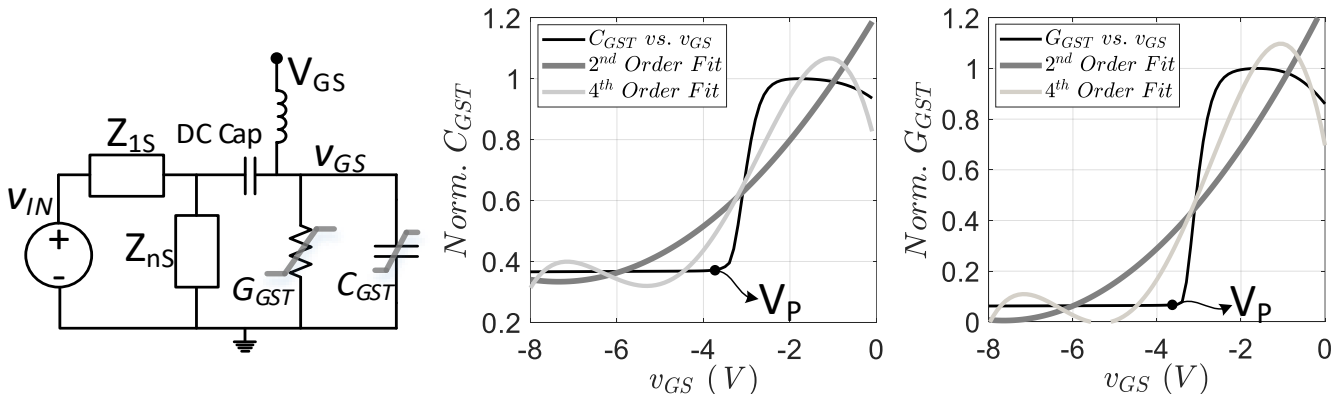

(a) (b) (c)

Fig. 2. (a) Simplified nonlinear gate equivalent circuit with source harmonic terminations, (b) normalized gate-source capacitance profile with v_{GS}, and (c) normalized gate-source conductance profile with v_{GS} of a typical GaN device.

A polynomial model is considered to represent the nonlinear profile of the C_{GST} and G_{GST} as

$$C_{GST} = C_0 + C_1 v_{GS} + C_2 v_{GS}^2 + C_3 v_{Gs}^3 + ... + C_n v_{Gs}^n \quad (3)$$

$$G_{GST} = G_0 + G_1 v_{GS} + G_2 v_{GS}^2 + G_3 v_{Gs}^3 + ... + G_n v_{Gs}^n \quad (4)$$

where C_0, C_1, C_2, C_n and G_0, G_1, G_2, G_n are the polynomial coefficients for capacitance and conductance, respectively. The polynomial coefficients are evaluated by curve fitting method. The second and fourth order fits are illustrated in Fig. 2(b) and 2(c). It is worth noting here that, although, fourth or higher order fits or a tan-hyperbolic function would predict closer nonlinear behavior, second order polynomials are considered in this analysis for simplicity without much compromise to the generality and accuracy of the end results. Due to such nonlinear profile and based on the source termination, the intrinsic gate voltage (v_{GS}) is distorted from the input sinusoidal voltage (V_{IN}). With second harmonic input non-linearity, the gate voltage waveform can be expressed as

$$v_{GS}(\theta) = V_{GS0} + V_1 \cos\theta + V_2 \cos(2\theta + \varphi_2)$$

$$v_{GS,\text{norm}}(\theta, \gamma, \varphi_2) = \frac{v_{GS}(\theta) - V_{GS0}}{V_1} = \cos\theta + \gamma \cos(2\theta + \varphi_2) \quad (5)$$

where V_1, V_2 are the fundamental and second harmonic gate voltage components, respectively, V_{GS0} is the gate-source bias voltage, and $v_{\text{GS,nom}}$ is the normalized intrinsic gate voltage. Two nonlinearity parameters, γ and φ_2, are defined to describe the impact of input nonlinearity in (5) where φ_2 is the phase difference between fundamental and second harmonic voltage components and $\gamma = V_2 / V_1$ is the input nonlinearity factor indicating second harmonic gate voltage magnitude with respect to fundamental. Different gate voltage waveforms for a few combinations of γ and φ_2 are shown in Fig. 1. The shape of the gate voltage waveform, as well as the conduction angle, are modified significantly by γ and φ_2 values [18]. The modified conduction angle, β, for a Class-B bias condition can be found by solving

$$\cos\frac{\beta}{2} + \gamma \cos(\beta + \varphi_2) = 0 \quad (6)$$

The variation of β with γ and φ_2 is shown in Fig. 3. It can be seen that the conduction angle can increase to ~230° or reduce

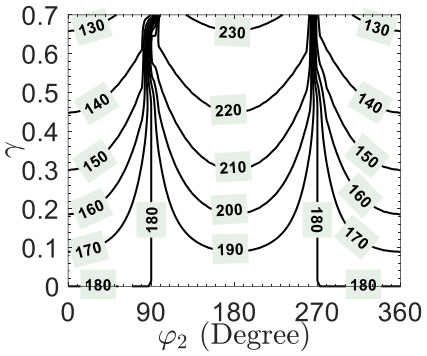

Fig. 3. Modified device conduction angle due to input nonlinearity.

to ~130° compared to the nominal bias conduction angle of 180° based on the input nonlinearity parameters. The deviation in conduction angle is translated into Class-F efficiency performance variation due to input nonlinearity which will be investigated in detail in the latter sections. However, it is worth noting here that the conduction angle is only reduced for the regions $0° \le \varphi_2 < 90°$ and $270° < \varphi_2 \le 360°$. In contrast, the conduction angle is increased in the region $90° < \varphi_2 < 270°$.

At this point, it is important to find the possible combinations of γ and φ_2 values which can be generated by the intrinsic nonlinearity of the device. To do so, the normalized gate-source current can be defined as

$$i_{GS}(\theta, \gamma, \varphi_2) = i_{C_{GST}}(\theta, \gamma, \varphi_2) + i_{G_{GST}}(\theta, \gamma, \varphi_2) \quad (7a)$$

$$i_{G_{GST}}(\theta, \gamma, \varphi_2) = G_{GST}.v_{GS,norm} = \left[G_0 + G_1 v_{GS,norm} + G_2 v_{GS,norm}^2\right] v_{GS,norm} \quad (7b)$$

$$i_{C_{GST}}(\theta, \gamma, \varphi_2) = \omega_0 \frac{d}{d\theta}\left[C_{GST}.v_{GS,norm}\right] = \omega_0 \frac{d}{d\theta}\left[C_0 + C_1 v_{GS,norm} + C_2 v_{GS,norm}^2\right] v_{GS,norm} \quad (7c)$$

where fundamental frequency of operation is defined as $f_0 = \omega_0/2\pi$. Considering a conjugate match at the fundamental frequency, second harmonic voltage and current components are of interest. By Fourier analysis of (5) and (7a), the normalized second harmonic voltage and current components can be calculated in terms of γ and φ_2 as

$$V_{2Sr}(\gamma, \varphi_2) = \gamma \cos(\varphi_2) \quad (8a)$$

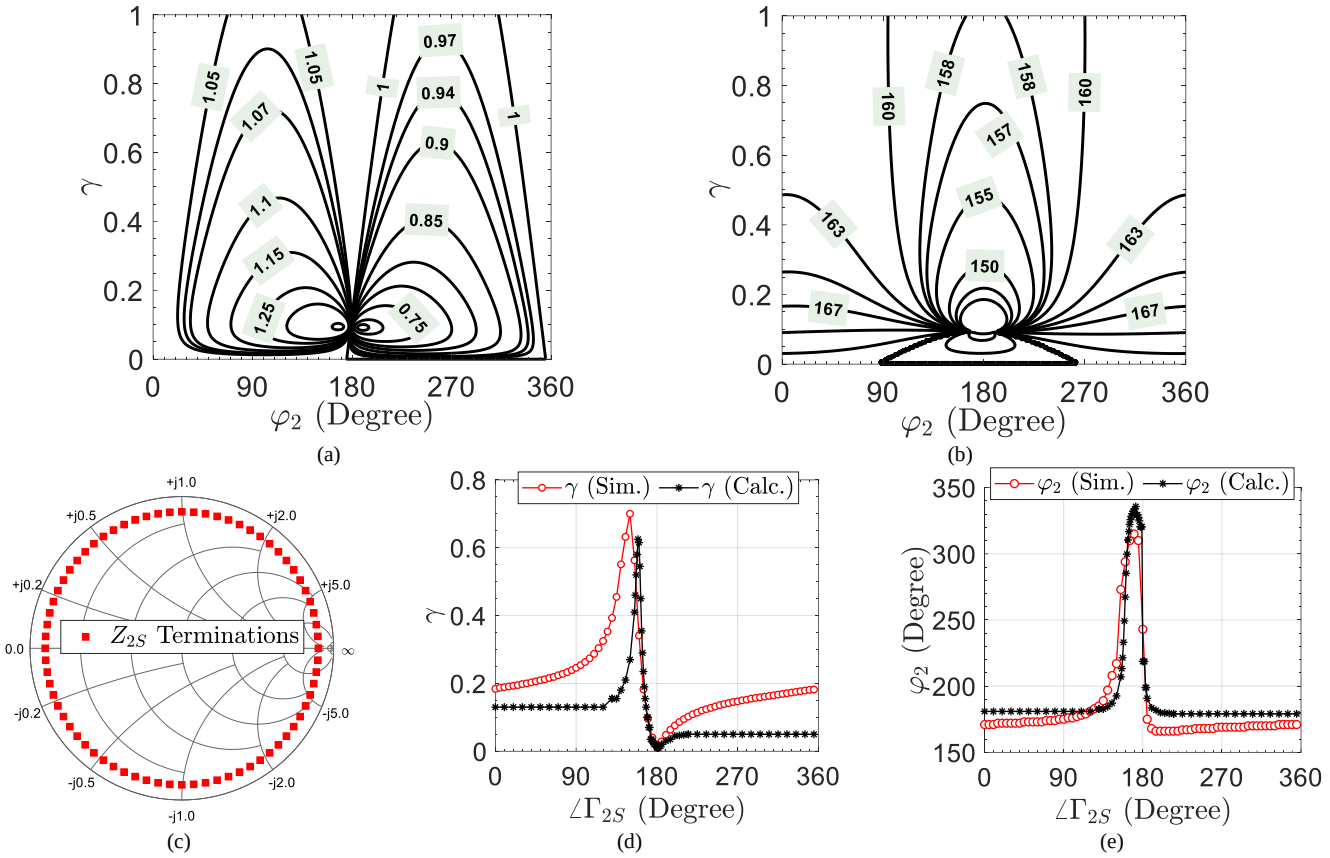

Fig. 4. Estimated (a) magnitude and (b) angle of Γ_{2S} for realizing different γ and φ_2 values at 1 GHz for a 2 mm GaN device, (c) simulated Z_{2S} terminations, simulated and calculated input nonlinearity parameters for Z_{2S} terminations with $|\Gamma_{2S}| = 0.9$: (d) γ and (e) φ_2.

$$V_{2Sq}(\gamma,\varphi_2) = -\gamma\sin(\varphi_2) \tag{8b}$$

$$I_{2Sr}(\gamma,\varphi_2) = \frac{G_1}{2} + \gamma\cos(\varphi_2)\left(G_0 + G_2 + \frac{G_2\left(3\gamma^2+2\right)}{4}\right) - \gamma\omega_0\sin(\varphi_2)\left(2C_0 + \frac{3C_2\left(\gamma^2+2\right)}{2}\right) \tag{8c}$$

$$I_{2Sq}(\gamma,\varphi_2) = -\gamma\sin(\phi_2)\left(G_0 + G_2 + \frac{G_2\left(3\gamma^2+2\right)}{4}\right) - C_1\omega_0 - \gamma\omega_0\cos(\phi_2)\left(2C_0 + \frac{3C_2\left(\gamma^2+2\right)}{2}\right) \tag{8d}$$

where V_{2Sr} and I_{2Sr} are the second harmonic real voltage and current components, and V_{2Sq} and I_{2Sq} are the second harmonic reactive voltage and current components, respectively. Thus, the second harmonic source impedance, Z_{2S}, can be estimated as a function of γ and φ_2 as

$$Z_{2S}(\gamma,\varphi_2) = -\frac{V_{2Sr}(\gamma,\varphi_2) - j.V_{2Sq}(\gamma,\varphi_2)}{I_{2Sr}(\gamma,\varphi_2) - j.I_{2Sq}(\gamma,\varphi_2)} \tag{9}$$

$$= \frac{-\gamma\left(\cos\varphi_2 + j\sin\varphi_2\right)}{\frac{G_1}{2} + \gamma\sigma_1\left(\cos\varphi_2 + j\sin\varphi_2\right) - \gamma\sigma_2\omega_0\left(\sin\varphi_2 - j\cos\varphi_2\right) - j\omega_0 C_1}$$

where

$$\sigma_1 = G_0 + G_2 + \frac{G_2\left(3\gamma^2+2\right)}{4}, \text{ and}$$

$$\sigma_2 = 2C_0 + \frac{3C_2\left(\gamma^2+2\right)}{2}.$$

From (9), the estimated magnitude and angle of second harmonic source reflection coefficient, Γ_{2S}, as functions of γ and φ_2 are illustrated at 1 GHz for a GaN 2-mm device in Fig. 4(a) and 4(b), respectively. Figure 4(a) and 4(b) bring in useful second harmonic source pull information and thus relate physical second harmonic input terminations to the nonlinear parameters γ and φ_2. For example, if $|\Gamma_{2S}| = 0.9$ contour line is considered in Fig. 4(a), the maximum $\gamma = 0.62$ can be achieved. It can also be seen that φ_2 values less than 180° result in $|\Gamma_{2S}|$ higher than unity, which implies that passive second harmonic source terminations can achieve φ_2 values only higher than 180° by exploiting the intrinsic input nonlinearity of a GaN device.

To validate the analyses, simulated γ and φ_2 values with a GaN 2 mm device are compared to the calculated ones for second harmonic source termination swept at the edge of the Smith chart as shown in Fig. 4(c) ($|\Gamma_{2S}| = 0.9$). The simulations are performed at constant 3 dB gain compression with fundamental source (Z_{1S}) conjugate matched, fundamental load (Z_{1L}) terminated at maximum efficiency point (MXE), and the second and third harmonic load (Z_{2L} and Z_{3L}) short circuited. The results are shown in Fig. 4(d) and (e). The simulated and calculated results are in excellent agreement. It is interesting to see that the input nonlinearity factor γ changes quite a bit from

0 to 0.6 which indicate significant conduction angle variation as can be predicted from Fig. 3. Besides, φ_2 is varied in the range of 180° to 330° unlike previous works [14]–[17] where it is considered fixed 180°. Since φ_2 value can be higher than 270°, the effective device conduction angle is reduced by the input nonlinearity and gate voltage shaping which can improve the PA efficiency performance.

The above analysis and validation provide an idea of achievable phase difference, φ_2, and input nonlinearity factor, γ, by passive second harmonic source terminations and by exploiting intrinsic input nonlinearity of the device. These predictions provide a realistic picture and a comprehensive understanding of achievable performance improvement or degradation in the subsequent analyses. To the best of authors' knowledge, this is the first time the input nonlinearity is modeled as a function of second harmonic source termination.

It is worth mentioning here that although this paper is limited to the intrinsic input nonlinearity and passive second harmonic source terminations ($|\Gamma_{2S}| \le 1$) where $\varphi_2 \ge 180°$, the scope of the analysis also covers the second harmonic input injection phenomenon where $|\Gamma_{2S}| > 1$. Therefore, a full range of φ_2 values from 0° to 360° can be achieved by input harmonic injection.

III. Input-Output Harmonic Engineered Class-F PA Analysis

Traditionally, input nonlinearity is avoided by presenting a harmonic short at the intrinsic gate node and the waveforms for Class-B tuned load condition are expressed as

$$v_{GS,B}(\theta) = V_{GS0} + V_1 \cos\theta \tag{10}$$

$$i_{DS,B}(\theta) = \begin{Bmatrix} \mathrm{I_{max}}\cos\theta,\ -\dfrac{\pi}{2} \le \theta \le \dfrac{\pi}{2} \\ 0,\ -\pi \le \theta \le -\dfrac{\pi}{2}, \dfrac{\pi}{2} \le \theta \le \pi \end{Bmatrix} \tag{11}$$

$$i_{DS,B}(\theta) = I_{DC,B} + \sum_{n=1}^{\infty} I_n \cos(n\theta)$$

where $\mathrm{I_{max}}$ is the maximum device current. On the other hand, the gate voltage waveform with second harmonic input nonlinearity is expressed as in (5). Depending on the γ and φ_2 values, the gate voltage waveforms are shaped and consequently, alter the drain current waveforms. The drain current waveforms with input nonlinearity can be deduced considering a constant trans-conductance device for a Class-B tuned load condition as

$$i_{DS}(\theta,\gamma,\varphi_2) = \begin{Bmatrix} \mathrm{I_{max}}[\cos\theta + \gamma\cos(2\theta+\varphi_2)],\ -\dfrac{\beta}{2} \le \theta \le \dfrac{\beta}{2} \\ 0,\ -\pi \le \theta \le -\dfrac{\beta}{2}, \dfrac{\beta}{2} \le \theta \le \pi \end{Bmatrix} \tag{12}$$

$$i_{DS}(\theta,\gamma,\varphi_2) = I_{DC} + \sum_{n=1}^{\infty} I_{nr}\cos(\mathrm{n}\,\theta) + \sum_{n=1}^{\infty} I_{nq}\sin(\mathrm{n}\,\theta)$$

where β is the modified conduction angle by gate voltage waveform shaping due to the second-order input nonlinearity, I_{DC} is the DC drain current component, and I_{nr}, I_{nq} are the real and reactive harmonic components of $i_{DS}(\theta)$, respectively.

For a classical Class-F PA, the second and third harmonic loads are terminated as a short circuit and an open circuit, respectively. Such harmonic termination results in theoretical drain efficiency of 90.7%. To derive the Class-F time-domain current waveforms accurately under input nonlinearity, it is important to make sure that the maximum drain current is limited to I_{max} with input-output harmonic terminations. Due to the open circuit third harmonic load termination, the third harmonic current cannot sustain; this is typically implemented by third harmonic current trapping technique [7]. However, under the presence of input nonlinearity i.e. at values other than $\gamma = 0$, the current expression in [7] does not hold which is further modified for non-zero γ values and for $\varphi_2 = \pi$ in [15] as

$$i_{DS,F}(\theta,\gamma) = \begin{Bmatrix} \dfrac{\mathrm{I_{max}}+\chi}{1+\gamma}[\cos\theta - \gamma\cos 2\theta] - \chi\cos 3\theta; -\dfrac{\beta}{2} \le \theta \le \dfrac{\beta}{2} \\ 0,\ -\pi \le \theta \le -\dfrac{\beta}{2}, \dfrac{\beta}{2} \le \theta \le \pi \end{Bmatrix} \tag{13}$$

where χ denotes the real third harmonic drain current coefficient, $i_3 = \chi\cos 3\theta$. This work presents the generalized formulation for time-domain Class-F drain current waveforms under input nonlinearity (i.e. any values of γ and φ_2) which is expressed as

$$i_{DS,F}(\theta,\gamma,\varphi_2) = \begin{Bmatrix} \varepsilon[\cos\theta + \gamma\cos(2\theta+\varphi_2)] - \\ \left(\chi\cos 3\theta - \xi\sin 3\theta\right),\ -\dfrac{\beta}{2} \le \theta \le \dfrac{\beta}{2} \\ 0,\ -\pi \le \theta \le -\dfrac{\beta}{2}, \dfrac{\beta}{2} \le \theta \le \pi \end{Bmatrix} \tag{14}$$

$$i_{DS,F}(\theta,\gamma,\varphi_2) = I_{DC} + \sum_{n=1}^{\infty} I_{nr}\cos(\mathrm{n}\,\theta) + \sum_{n=1}^{\infty} I_{nq}\sin(\mathrm{n}\,\theta)$$

where χ, ξ denote the coefficients for real and reactive terms of third harmonic drain current, $i_3 = \chi\cos 3\theta - \xi\sin 3\theta$, respectively. The current limiting factor ε is defined as

$$\varepsilon = \frac{\mathrm{I_{max}} + \chi\cos 3\theta_{\mathrm{m}} - \xi\sin 3\theta_{\mathrm{m}}}{\cos\theta_{\mathrm{m}} + \gamma\cos\left(2\theta_{\mathrm{m}} + \varphi_2\right)} \tag{15}$$

where θ_{m} is the angle for which $i_{DS,F} = I_{max}$. The current limiting factor ε ensures the maximum drain current is limited to $\mathrm{I_{max}}$ at any γ and φ_2 values. It is worth mentioning here that the classical Class-F drain current (source second harmonic short circuited) does not contain any third harmonic components at Class-B bias condition and exclusion of third harmonic component is not typically needed. However, a second harmonic source termination other than a short circuit alters the drain current waveforms from a typical half sinusoid and results in both real and reactive third harmonic drain current components.

The coefficients χ and ξ can be calculated as a function of β, γ, and φ_2 by equating the real (I_{3r}) and imaginary (I_{3q}) part of the third harmonic current to zero as

$$I_{3r} = \frac{1}{\pi}\int_{-\beta/2}^{+\beta/2} i_{DS,F}(\theta,\gamma,\varphi_2).\cos 3\theta\ d\theta = 0 \tag{16a}$$

$$I_{3q} = \frac{1}{\pi}\int_{-\beta/2}^{+\beta/2} i_{DS,F}(\theta,\gamma,\varphi_2).\sin 3\theta\ d\theta = 0 \tag{16b}$$

From (13-15), χ and ξ are calculated as functions of β, γ, and φ_2 as

$$\chi(\beta,\gamma,\varphi_2) = \frac{\left[\mathrm{I_{max}} - \xi sin3\theta_m\right]\left[15\sigma_5 + 12\sigma_4\gamma cos\varphi_2\right]}{10\sigma_3\sigma_6 - 3cos3\theta_{\mathrm{m}}\left(5\sigma_5 + 4\sigma_4\gamma\cos\varphi_2\right)} \tag{17}$$

$$\xi(\beta,\gamma,\varphi_2)=\frac{12\delta_4\sigma_6\gamma I_{max}\sin\varphi_2}{\left[\begin{array}{l}5\delta_6\left(2\sigma_3\sigma_6-3\sigma_5\cos3\theta_m\right)-12\gamma.\\\left(\sigma_4\delta_6\cos\varphi_2\cos3\theta_m-\delta_4\sigma_6\sin\varphi_2\sin3\theta_m\right)\end{array}\right]} \quad (18)$$

where,

$\sigma_3=cos\theta_m+\gamma cos\left(2\theta_m+\varphi_2\right)$,

$\sigma_4=5sin\frac{\beta}{2}+sin\frac{5\beta}{2}$, $\delta_4=5sin\frac{\beta}{2}-sin\frac{5\beta}{2}$

$\sigma_5=2sin\beta+sin2\beta$, $\delta_5=2sin\beta-sin2\beta$, and

$\sigma_6=3\beta+sin3\beta$, $\delta_6=3\beta-sin3\beta$.

The variation of normalized χ and ξ with input nonlinearity parameters, γ and φ_2, are shown in Fig. 5(a) and (b). Both χ and ξ have zero value at γ = 0 which converges to the classical Class-F condition. This ensures the accuracy of the analytical results.

By replacing (17) and (18) into (14), the time-domain drain current components are evaluated for different γ and φ_2. The DC and fundamental drain current components are computed from (14) as

$$I_{DC}(\beta,\gamma,\varphi_2)=\frac{\varepsilon}{\pi}\left[\sin\frac{\beta}{2}+\frac{\gamma\cos\varphi_2}{2}\sin\beta\right]-\frac{\chi}{3\pi}\sin\frac{3\beta}{2} \quad (19)$$

$$I_{1r}(\beta,\gamma,\varphi_2)=\frac{\varepsilon}{2\pi}(\beta+\sin\beta)-\frac{\chi\left[\sin2\beta+2\sin\beta\right]}{4\pi}+\frac{\varepsilon\gamma\cos\varphi_2}{3\pi}\left[3\sin\frac{\beta}{2}+\sin\frac{3\beta}{2}\right] \quad (20)$$

$$I_{1q}(\beta,\gamma,\varphi_2)=\frac{\xi}{4\pi}\delta_5-\frac{\varepsilon\gamma\sin\varphi_2}{3\pi}\left[3\sin\frac{\beta}{2}-\sin\frac{3\beta}{2}\right] \quad (21)$$

where I_{DC}, I_{1r}, and I_{1q} are the DC, and fundamental real, and reactive drain current components, respectively. It is worthwhile noting that the reactive fundamental drain current component is not zero unlike classical Class-F PA. This is due to the drain current waveform shaping by input nonlinearity. When input harmonics are short circuited, i.e. γ = 0, reactive current components become zero, converges to the typical Class-F PA without input nonlinearity.

To compute the output power and efficiency of a Class-F power amplifier, the drain voltage is considered as [2]

$$v_{DS,F}(\theta)=V_{DD}-\left(V_{DD}-V_K\right)\left(\frac{2}{\sqrt{3}}\cos\theta-\frac{1}{3\sqrt{3}}\cos3\theta\right) \quad (22)$$

where V_{DD}, and V_K are the drain supply voltage and knee voltage, respectively. Thus, the DC power, output power, and drain efficiency of a Class-F PA as functions of input nonlinearity parameters γ and φ_2 can be predicted as

$$P_{DC}(\beta,\gamma,\varphi_2)=\mathrm{V_{DD}}\times I_{DC}(\beta,\gamma,\varphi_2) \quad (23)$$

$$\mathrm{P_{OUT}}(\beta,\gamma,\varphi_2)=\frac{1}{2}\times\frac{2}{\sqrt{3}}(\mathrm{V_{DD}}-\mathrm{V_K})\times I_{1r}(\beta,\gamma,\varphi_2) \quad (24)$$

$$\eta(\beta,\gamma,\varphi_2)=\frac{\frac{1}{2}\times\frac{2}{\sqrt{3}}(\mathrm{V_{DD}}-\mathrm{V_K})\times I_{1r}(\beta,\gamma,\varphi_2)}{\mathrm{V_{DD}}\times\mathrm{I_{DC}}(\beta,\gamma,\varphi_2)} \quad (25)$$

The analytical results of a Class-F PA under input nonlinearity are summarized in Table I for a few special cases. For γ = 0, the performance converges to the classical Class-F ones. As expected, the Class-F performance can be enhanced or degraded based on the input nonlinearity.

TABLE I
SUMMARY OF THE ANALYTICAL RESULTS OF A CLASS-F PA UNDER INPUT NONLINEARITY

Parameters	γ = 0	γ = 0.5	
		$\varphi_2=\pi$	$\varphi_2=2\pi$
I_{DC}	$1/\pi$	0.43	0.33
I_1	1/2	0.48	0.54
V_1^+	$2/\sqrt{3}$	$2/\sqrt{3}$	$2/\sqrt{3}$
Pout*	1	0.96	1.08
Efficiency	90.7%	64.5%	94.5%

+Normalized to (V_{DD}-V_K)
*Normalized to classical Class-F output power

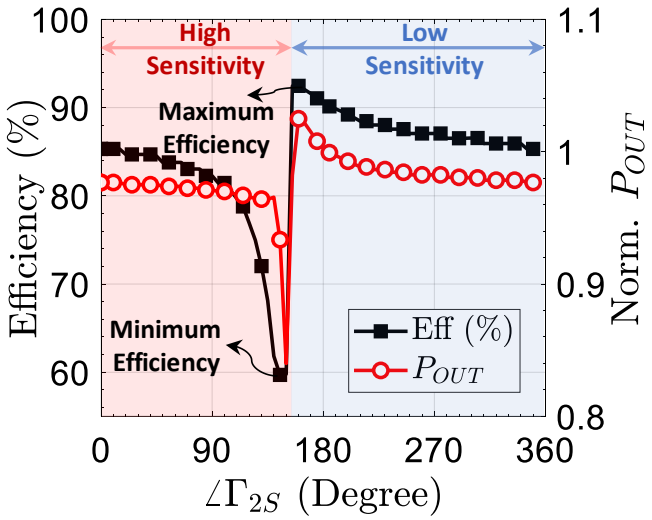

Fig. 5. Theoretical prediction of second harmonic source pull- efficiency and output power variation of a Class-F PA with different second harmonic input terminations ($|\Gamma_{2S}|$ = 0.9) at 1 GHz.

To assess the realistic performance with the intrinsic input nonlinearity of a GaN device, efficiency and output power can be predicted as a function of Z_{2S} from (9), (24) and (25) for constant $|\Gamma_{2S}|$ = 0.9 circle. The predicted Class-F PA performance with input second harmonic termination (second harmonic source pull) is shown in Fig. 5. Both efficiency and output power are significantly varied by the input nonlinearity. It is worth noting that the maximum theoretical efficiency achieved is 93.3% at $\angle\Gamma_{2S}$ =160° compared to the traditional Class-F PA efficiency of 90.7% (short circuit, $\angle\Gamma_{2S}$ =180°). On the other hand, the efficiency is severely degraded to 57% at $\angle\Gamma_{2S}$ =150°. These analytical results suggest that a Class-F PA should be carefully designed considering the impact of input nonlinearity and proper Z_{2S} termination should be presented to achieve optimum Class-F PA performance. On the other hand, the normalized output power remains almost constant but varies from 0.85-1.05 compared to the nominal Class-F PA. Overall, the Z_{2S} terminations from $\angle\Gamma_{2S}$ =0° to $\angle\Gamma_{2S}$ =150° (inductive Z_{2S} terminations) present high sensitive design space while the Z_{2S} terminations from $\angle\Gamma_{2S}$ =160° to $\angle\Gamma_{2S}$ =360° (mostly capacitive Z_{2S} terminations) present relatively less variation and safe design space. Understanding such impact of Z_{2S} terminations are quite useful for the designers targeting mass production. It in fact allows the designer an additional degree of freedom in

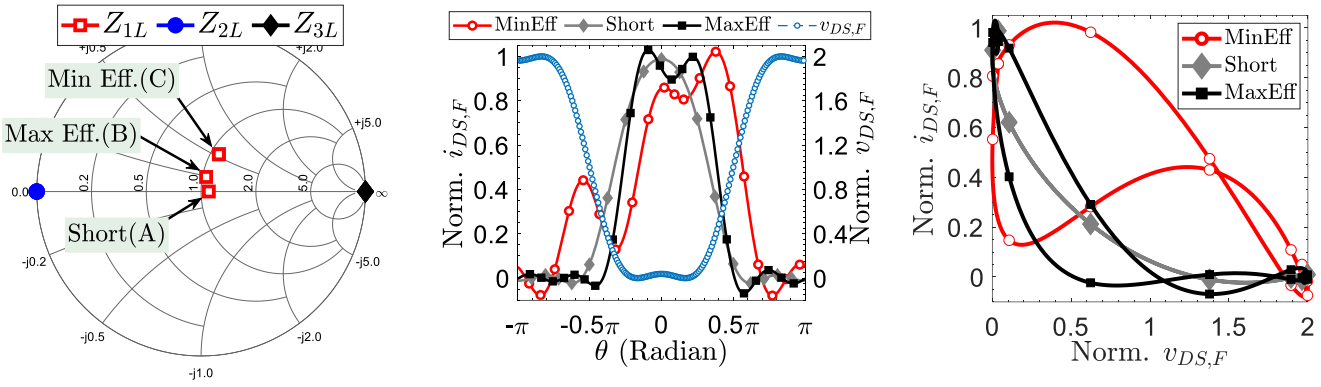

(a) (b) (c)

Fig. 6. Class-F: (a) variation of optimum fundamental load terminations for different Z_{2S} terminations, (b) drain voltage and current waveforms, and (c) load lines for the Z_{2S} terminations at short, minimum efficiency, and maximum efficiency. The drain voltage and drain current are normalized to V_{DD} and I_{max}, respectively.

realizing the input matching network in the context of variability or limited values of available components or to consider process variation in fully integrated designs.

The resulting load impedance terminations for Class-F PA with input nonlinearity can be computed as

$$Z_{nL} = -\frac{V_{nr} - V_{nq}}{I_{nr} - I_{nq}} \quad (26)$$

where Z_{nL} is the n^{th}-harmonic load impedance termination, and V_{nr}, V_{nq} are the n^{th}-harmonic real and reactive voltage components, respectively. As the points of interest, the load terminations (up to third harmonics) for points A (Short), B (Max. Eff), and C (Min. Eff.) are calculated and shown in Fig. 6(a). It is no surprise that the optimum fundamental impedance with input nonlinearity defined as

$$Z_{1L,OPT}(\beta,\gamma,\varphi_2) = R_{1L,OPT}(\beta,\gamma,\varphi_2) + jX_{1L,OPT}(\beta,\gamma,\varphi_2) \quad (27)$$

is not always real; rather, it can be complex and differed from the typical Class-F optimum load impedance which is purely resistive. This is due to the current waveform shaping by the input nonlinearity. These variations suggest that the fundamental impedance termination must be readjusted with input nonlinearity so that optimum Class-F PA performance is achieved. The reconstructed current waveforms with the Fourier components are illustrated in Fig. 6(b). It can be seen that the conduction angle of the drain current is reduced at the maximum efficiency point and increased at the minimum efficiency point as expected compared to the short one. To keep the drain voltage as square shaped as shown in Fig. 6(b), the optimum fundamental load terminations have been adjusted. The corresponding load lines are illustrated in Fig. 6(c). It is worth noting that the load line excursion at the minimum efficiency point hits the higher stress area of the device which affects device lifetime and compromises device reliability.

IV. Load Pull Measurements and Practical Validation

In this work, vector load pull (VLP) measurements are performed to validate the theoretical analyses presented. A VLP setup and measurement provide useful information about device input characteristics which enhances measurement accuracy. The vector network analyzer (VNA) based VLP measurement setup is shown in Fig. 1. The setup consists of a load tuner MPT 1808, a source tuner MPT Lite 1808 and a phase reference unit Mesuro PR-50 from Focus Microwaves Group, VNA ZVA67 and its extension unit ZVAX-TRM40 from Rohde & Schwarz, a spectrum analyzer MS2840A from Anritsu, and DC power supplies E3634A from Agilent. The load tuner can tune the fundamental (Z_{1L}), second (Z_{2L}) and third (Z_{3L}) harmonic loads from 0.8 GHz to 18 GHz. The source tuner does the same for fundamental (Z_{1S}) and second (Z_{2S}) harmonic source impedances. To communicate, control and for synchronized measurements, Focus Device Characterization Suite (FDCS) [25] software is used. The setup mainly consists of two calibration steps. Firstly, tuner calibration and then wave calibration. The tuners are calibrated with the FDCS software using VNA ZVA67. For wave calibration, Mesuro calibration software is used along with the Mesuro phase reference unit PR-50 and a power meter NRP2 with power sensor NRP Z57 from Rohde & Schwarz. For wave measurements, both wave power and phase calibration are performed by Mesuro calibration software.

A. VLP Measurement Results

To validate the theoretical framework presented in the previous Section II and III, pulsed VLP measurements are performed with a GaN 2 mm at 1 GHz. However, to perform accurate load pull measurements and to probe intrinsic parameters, device parasitics especially the drain to source capacitance (C_{DS}) is needed to be de-embedded. Once the parasitic information is extracted accurately, the impact of second harmonic source pull is investigated for a Class-F PA. It is performed in the following three steps:

- Terminate second harmonic source (Z_{2S} or Γ_{2S}) to short and do a fundamental load pull for the Class-F operation loading condition i.e. second harmonic at short and third harmonic at open. Find the maximum efficiency points.
- Perform a second harmonic source pull by terminating fundamental load at the maximum efficiency point found in step 1 and maintaining Class-F harmonic load terminations.
- Since, a second harmonic source termination can alter the optimum fundamental load termination significantly, redo a fundamental load pull at each second harmonic source

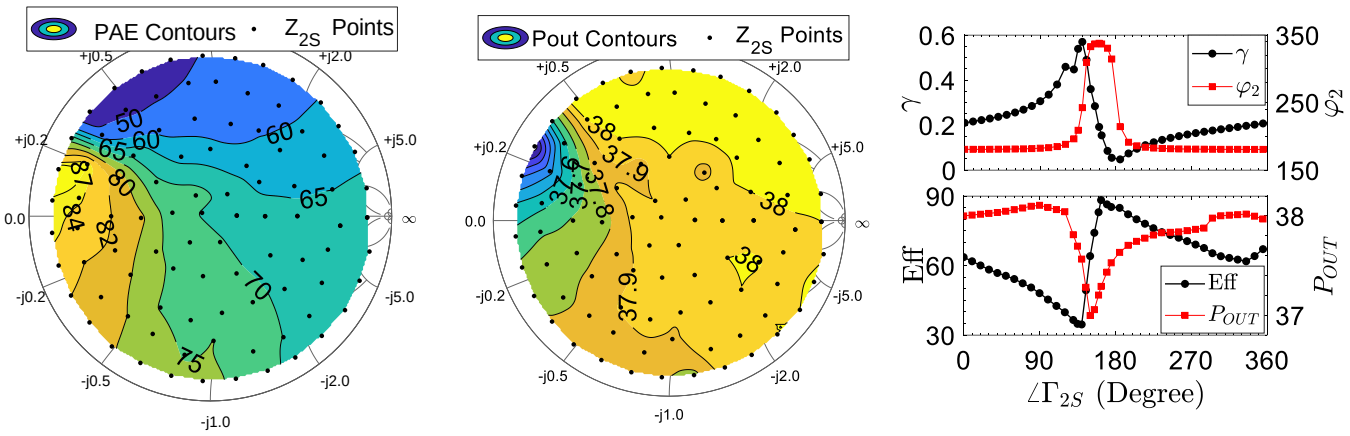

Fig. 7. (a) Efficiency contours, (b) output power contours with second harmonic source pull, and (c) variation of input nonlinearity parameters (γ and φ_2), efficiency, and output power with second harmonic source terminations ($|\Gamma_{2S}| = 0.9$).

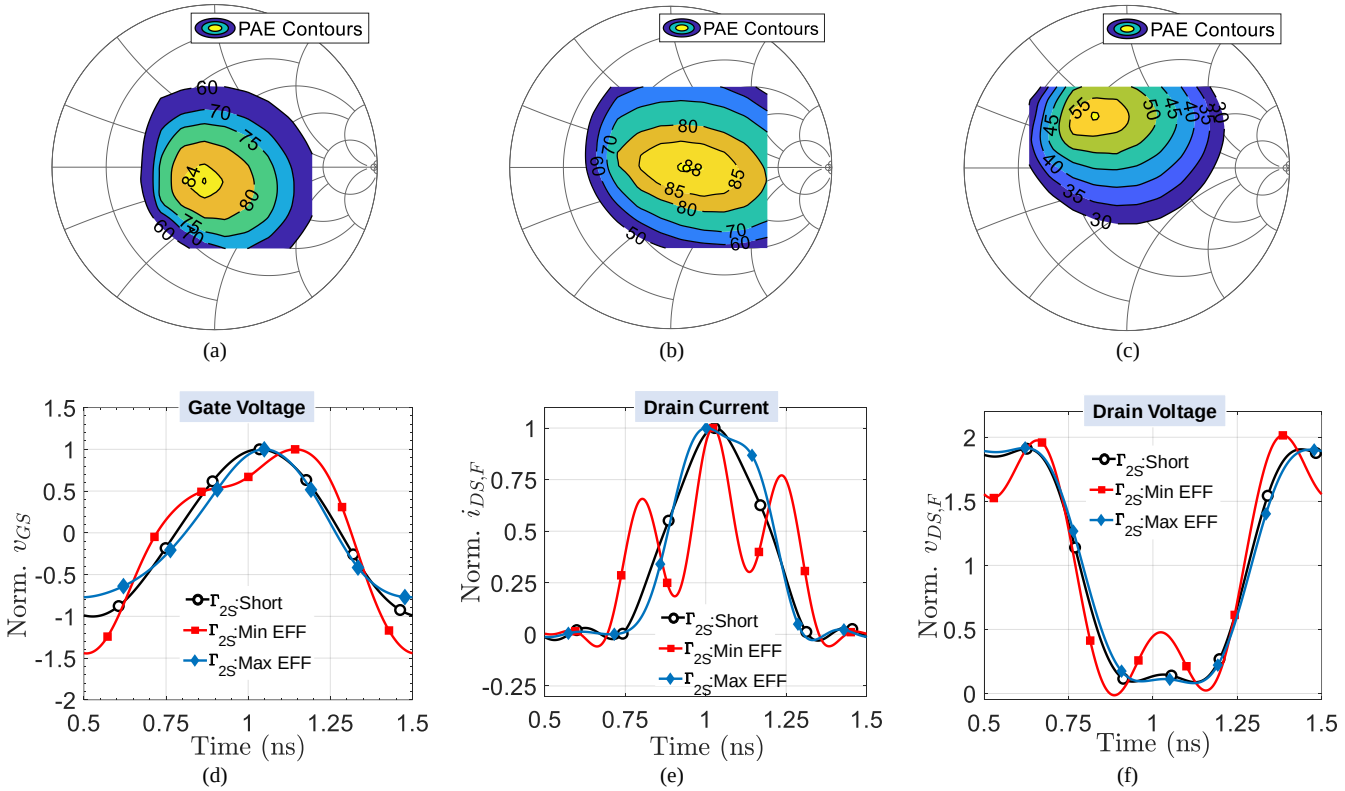

Fig. 8. Fundamental load pull efficiency contours for Z_{2S} terminations: (a) short, (b) maximum efficiency, (c) minimum efficiency, and waveforms: (d) gate voltage, (e) drain current, and (f) drain voltage.

termination to find its actual performance.

Following Step 1 mentioned above, the second harmonic source pull results are performed with Z_{1L} terminated fixed at maximum efficiency (MXE) load and the results are shown in Fig. 7. The maximum $|\Gamma_{2S}|$ realized at the intrinsic gate node for second harmonic source pull is about 0.9 due to the loss of the couplers, coaxial cables, probes and device parasitics. As predicted in theoretical sections, the efficiency performance of a Class-F PA is significantly impacted by the second harmonic source termination as can be seen from Fig. 7(a). The measured efficiency is varied in the range of 35% to 88%. On the other hand, the output power varies within a dB with the variation of input second harmonic termination over the full Smith chart as shown in Fig. 7(b). To have a closer look, the variation of output power, efficiency, and input nonlinearity parameters (γ and φ_2) for $|\Gamma_{2S}| = 0.9$ are shown in Fig. 7(c). Both γ and φ_2 profiles show similar trends to the simulated and calculated ones. The φ_2 values for different Z_{2S} terminations are higher than 166° which is calculated as 180° in Section II. Besides, the maximum value of the input nonlinearity factor γ is measured to be ~0.57 which is analytically predicted about 0.62. Moreover, the efficiency and output power variation with Z_{2S} termination follows similar trends as predicted theoretically in Fig. 5. To evaluate the efficiency and output power performance, we define three points of interest: A) $\angle\Gamma_{2S} = 180°$- nominal Class-F operation, B) $\angle\Gamma_{2S} = 160°$- maximum efficiency operation, and C) $\angle\Gamma_{2S} = 140°$- minimum efficiency operation. The Z_{2S}

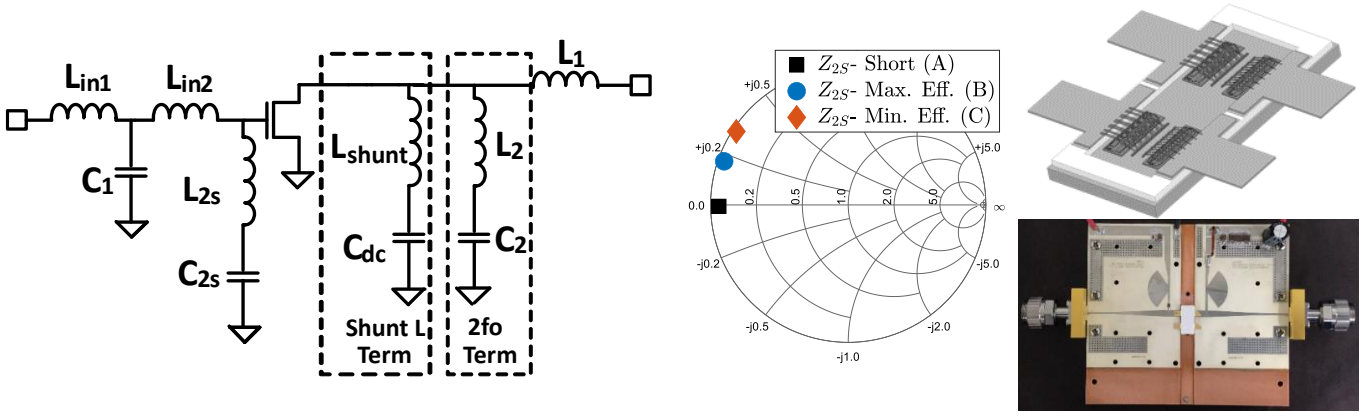

(a) (b) (c)

Fig. 9. (a) Schematic of the input-output pre-match network for 24mm GaN device, (b) implemented three Z_{2S} termination for three different GaN 24 mm devices (Z_0 = 3.5 Ω), and (c) in-package input harmonic terminated prematched GaN 24 mm power device and high power fixture used for verification for GaN devices with diferent Z_{2S} terminations.

termination at $\angle\Gamma_{2S}$ = 140° where the input nonlinearity factor γ is maximum results in the minimum efficiency about 35% which is 85% at $\angle\Gamma_{2S}$ = 180° and 88.2% at $\angle\Gamma_{2S}$ = 160°. It is also clear that the intrinsic source second harmonic short is not the optimum termination for the Class-F PA efficiency performance. The optimum termination is indeed a termination at $\angle\Gamma_{2S}$ = 160° where efficiency is about 3.2% higher than a short termination.

As the optimum fundamental load is significantly altered by different Z_{2S} terminations as predicted in Section III and illustrated in Fig. 6(a), it is important to redo a fundamental load pull at every Z_{2S} terminations to find true efficiency performance. The fundamental load pull is performed at $\angle\Gamma_{2S}$ = 180°, 160°, and 140° as shown in Fig. 8(a-c). It can be seen that the optimum fundamental load impedance is different for different Z_{2S} terminations which are in excellent agreement to the theoretical prediction illustrated in Fig. 6(a). Moreover, it is worth noting here that fundamental retuning improves efficiency performance at $\angle\Gamma_{2S}$ = 140° in Fig. 8(c) from 35% to 57% which is predicted analytically about 60% in Fig. 5. However, it should be noted that still there is an efficiency minimum at $\angle\Gamma_{2S}$ = 140° with an efficiency delta of ~30% which has not been compensated by fundamental retuning.

The gate voltage, drain current, and drain voltage waveforms are shown in Fig. 8(d-f). At Z_{2S} short termination, the gate voltage waveform is sinusoidal as expected. The gate voltage waveform is shaped wide at Z_{2S} terminations that result in minimum efficiency as predicted analytically. Thus, the drain current conduction angle is also increased as shown in Fig. 8(e). On the other hand, the gate voltages and drain currents are contracted comparatively for the Z_{2S} terminations that provide the maximum efficiency. It is worth noting that the current waveforms at short, minimum efficiency and maximum efficiency resemble well to the theoretically reconstructed current waveforms presented in Fig. 6(b). The drain voltage waveforms are shaped rectangular for the Class-F load terminations and remains almost unaltered for different Z_{2S} terminations as predicted analytically in Section III.

B. *High Power Implementation*

Once the Z_{2S} design space is identified for Class-F PA operation, input and output matching networks can be designed to leverage the combined benefits of input-output harmonic tuning. To showcase the theoretical findings as applied to high power applications, a large periphery GaN device (24 mm) is mounted in a high-power air cavity package with pre-matching components fabricated from integrated passive devices (IPDs) for 2.2 GHz operation. Bond wires are used into interconnect between package leads, IPDs and GaN die to realize load and source terminations. Figure 9(a) shows the input and output in-package pre-matching network, where the bond wire component L_{2s} was varied to create different 2nd harmonic source terminations [26]. The second and third harmonic load are terminated at short and open circuit, respectively, to realized Class-F mode of operation at 2.2 GHz. The entire packaged GaN device with IPDs was modelled in a full wave electromagnetic simulator accounting for bond wires and package parasitics to allow for the determination of the source harmonic termination. Figure 9(b) shows the resulting source impedance for three cases of interest: short circuit (A-typical Class-F), maximum drain efficiency (B), and minimum drain efficiency (C). Three GaN 24 mm devices are implemented for these three Z_{2S} terminations. The output pre-match IPD was designed to keep the output second harmonic terminations at short and third harmonic at open circuit condition for all three cases at 2.2 GHz. The three devices are measured and verified on a high-power passive load pull apparatus. The device and its test fixture used for validation are shown in Fig. 9(c). The load pull efficiency and output power contours at 2.2 GHz with constant 3-dB gain compression level for three Z_{2S} terminations are shown in Fig. 10 for three different cases of Z_{2S} terminations. The measurements are performed with a fixed drain supply of 48 V and a quiescent drain current of 237 mA. The RF signal excitation is pulsed with a duty cycle of 10% to measure the high power PA performance. It is worth noting here that the optimum fundamental loads vary due to different Z_{2S} terminations as predicted by theoretical analysis and also observed in the low power load pull measurements. The power sweep results for the three different cases are shown in Fig. 11.

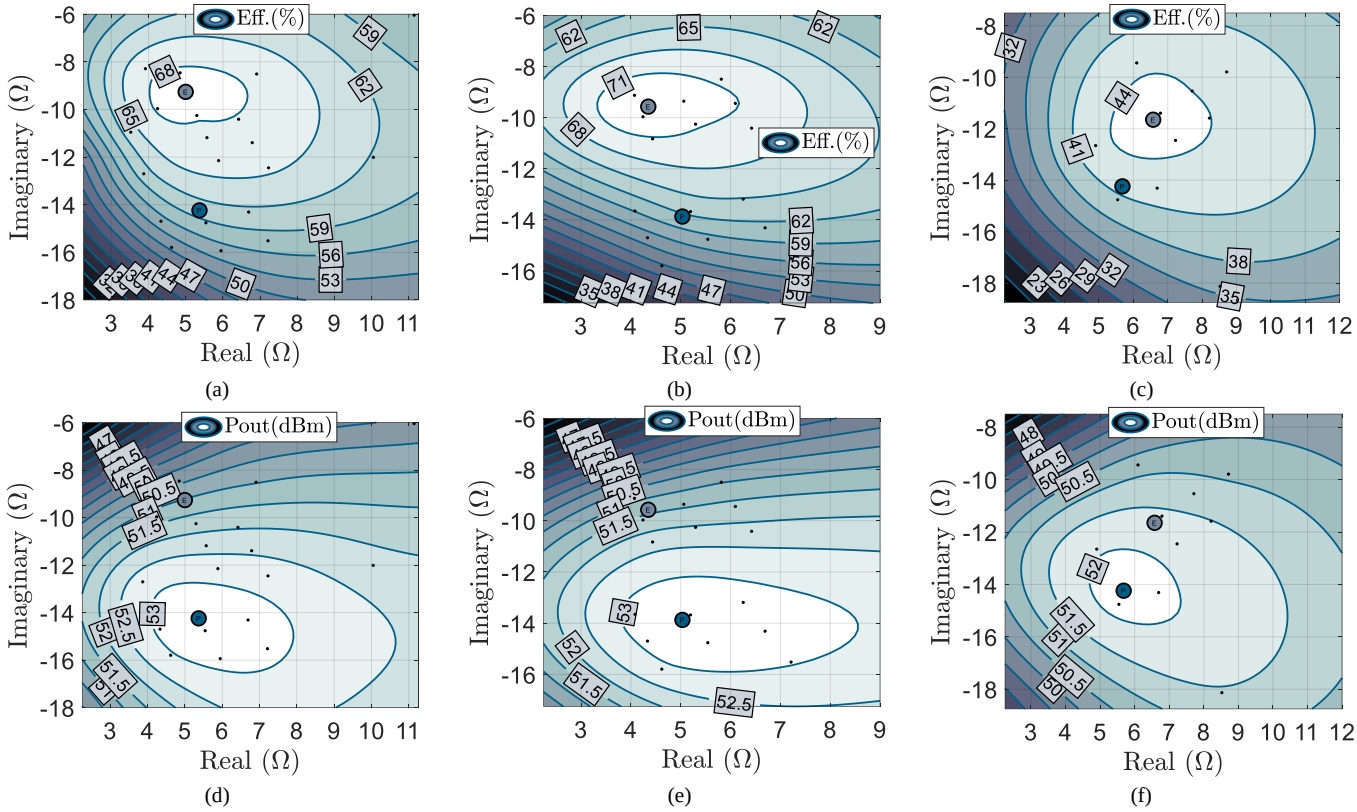

Fig. 10. Efficiency and output power contours of the GaN 24 mm device for different Z_{2S} terminations: (a, d) short, (b, e) maximum efficiency, and (c, f) minimum efficiency.

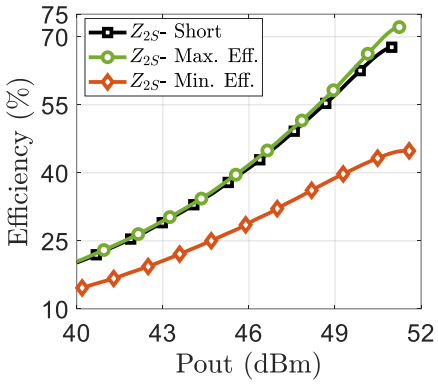

Fig. 11. Power sweep measurement results of the three GaN 24 mm devices with different Z_{2S} terminations. Fundamental load impedances were terminated at the MXE points.

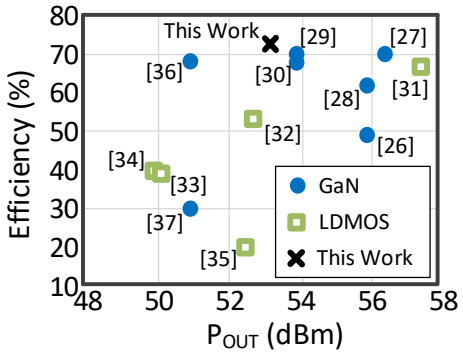

Fig. 12. Proposed high power GaN device performance at maximum efficiency point compared to the previous works.

TABLE II
SUMMARY OF THE GAN 24 MM DEVICE PERFORMANCE WITH INPUT NONLINEARITY

Z_{2S}	γ	φ_2 (Degree)	Measured Efficiency (%)	Measured Δ_{EFF} (%)$^+$	Predicted Efficiency* (%)	Predicted Δ_{EFF} (%)$^+$
Max. Eff.	0.45	280	72.1	4.4	83.4	1.8
Min. Eff.	0.6	216	45	-22.7	57.8	-23.8
Short	<0.05	250	67.7	0	81.6	0

* Assumed V_{knee} = 10% V_{DD}
$^+$ $\Delta_{EFF} = \eta - \eta(Z_{2S} = 0)$.

TABLE III
SUMMARY OF THE PROPOSED INPUT-OUTPUT HARMONIC TUNED GAN 24 MM DEVICE PERFORMANCE COMPARED TO THE RECENT WORKS

Ref.	Year	Tech.	Freq. (GHz)	Pout (dBm)	Eff. (%)
[27]	2006	GaN	1.5	56	49
[28]	2018	GaN	2.45	56.5	70
[29]	2018	GaN	0.36	56	62
[30]	2014	GaN	2.14	54	70
[31]	2018	GaN	2.35	54	68
[37]	2015	GaN	1.94	51	68.1
[38]	2018	GaN	2	51	30
This Work	**2020**	**GaN**	**2.2**	**53.3**	**72.1**

The efficiency measured by the Z_{2S} termination at point B is 72.1% compared to the nominal 67.7% Class-F performance which is about 4.4% efficiency improvement. On the other hand, the efficiency is degraded to 45% by the Z_{2S} termination at point C. The maximum output power (MXP) for three different cases are found to be 53.24 dBm (point A), 53.3 dBm

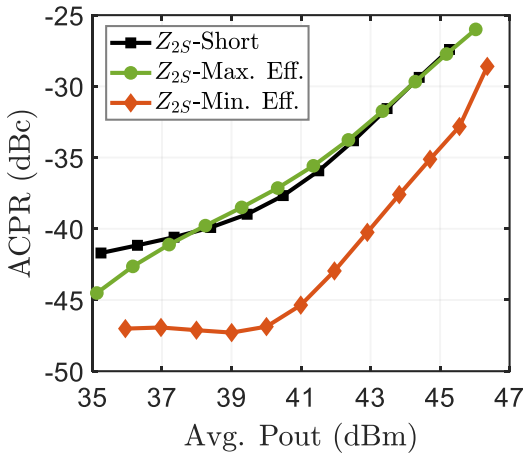

Fig. 13. Linearity performance of the PA with a 20 MHz LTE signal.

(point B), 52.16 dBm (point C). The performance of the Class-F high power device with input nonlinearity at 2.2 GHz is summarized in Table II. The difference in absolute efficiency numbers of the predicted and measured results can be attributed to the frequency dispersion of the device performance. In this context, efficiency delta, $\Delta_{EFF} = \eta - \eta(Z_{2S} = 0)$, is considered as a measure of comparison. It can be seen that the predicted Δ_{EFF} results align well with the measured ones. The input-output harmonic controlled high power Class-F GaN device performance compared to the previous works [27]–[38] is listed in Table III. The improvement of a few percent points by utilizing source harmonic control assists in realizing higher efficiency device performance as illustrated in Fig. 12 which is highly appreciated especially at high power operation. To investigate the linearity performance, output power and adjacent channel power ratio (ACPR) are evaluated for three different Z_{2S} terminations in response to a long-term evolution (LTE) 20 MHz signal with 7.5 dB peak to average power ratio (PAPR). The ACPR performance versus output power is shown in Fig. 13. It can be seen that the nonlinearity performance for maximum efficiency Z_{2S} termination is comparable to the short-circuit Z_{2S} termination.

V. Conclusions

This work presents an in-depth analysis and modelling of a Class-F PA with input and output harmonic tuning. For the first time, theoretical analyses relating the generation of input nonlinearity with second harmonic source termination are presented. Thereafter, the performance of a Class-F PA is analytically investigated with input and output harmonic tuning and the favourable as well as the adverse regions for second harmonic source terminations are identified. The analyses are first validated with VLP measurements using a low power GaN 2 mm device. Further, a high power GaN 24 mm PA with in-package second harmonic source terminations are implemented as a proof of concept operating at 2.2 GHz. An efficiency improvement of 4.4% is measured by exploiting optimum second harmonic source and load terminations.

References

[1] A. Grebennikov and F. H. Raab, "History of Class-F and Inverse Class-F Techniques: Developments in High-Efficiency Power Amplification from the 1910s to the 1980s," *IEEE Microw. Mag.*, vol. 19, no. 7, pp. 99–115, Nov. 2018.

[2] P. Colantonio, F. Giannini, and E. Limiti, *High Efficiency RF and Microwave Solid State Power Amplifiers*. John Wiley & Sons, 2009.

[3] F. H. Raab, "Class-F power amplifiers with maximally flat waveforms," *IEEE Trans. Microw. Theory Tech.*, vol. 45, no. 11, pp. 2007–2012, Nov. 1997.

[4] P. Colantonio, F. Giannini, G. Leuzzi, and E. Limiti, "Multiharmonic manipulation for highly efficient microwave power amplifiers," *Int. J. RF Microw. Comput.-Aided Eng.*, vol. 11, no. 6, pp. 366–384, Nov. 2001.

[5] F. H. Raab, "Maximum efficiency and output of class-F power amplifiers," *IEEE Trans. Microw. Theory Tech.*, vol. 49, no. 6, pp. 1162–1166, Jun. 2001.

[6] P. J. Tasker, "Practical waveform engineering," *IEEE Microw. Mag.*, vol. 10, no. 7, pp. 65–76, Dec. 2009.

[7] J. H. Kim, G. D. Jo, J. H. Oh, Y. H. Kim, K. C. Lee, and J. H. Jung, "Modeling and Design Methodology of High-Efficiency Class-F and Class-F^{-1} Power Amplifiers," *IEEE Trans. Microw. Theory Tech.*, vol. 59, no. 1, pp. 153–165, Jan. 2011.

[8] J. Moon, S. Jee, J. Kim, J. Kim, and B. Kim, "Behaviors of Class-F and Class-F^{-1} Amplifiers," *IEEE Trans. Microw. Theory Tech.*, vol. 60, no. 6, pp. 1937–1951, Jun. 2012.

[9] T. Sharma *et al.*, "Simplified First-Pass Design of High-Efficiency Class-F^{-1} Power Amplifiers Based on Second-Harmonic Minima," *IEEE Trans. Microw. Theory Tech.*, pp. 1–15, 2019.

[10] T. Sharma *et al.*, "Novel High Efficiency Power Amplifier Mode Using Open Circuit Harmonic Loading," in *2019 IEEE MTT-S International Microwave Symposium (IMS)*, 2019, pp. 79–82.

[11] H. Jang, P. Roblin, and Z. Xie, "Model-Based Nonlinear Embedding for Power-Amplifier Design," *IEEE Trans. Microw. Theory Tech.*, vol. 62, no. 9, pp. 1986–2002, Sep. 2014.

[12] P. Colantonio, F. Giannini, G. Leuzzi, and E. Limiti, "Theoretical facet and experimental results of harmonic tuned PAs," *Int. J. RF Microw. Comput.-Aided Eng.*, vol. 13, no. 6, pp. 459–472, Oct. 2003.

[13] T. Sharma *et al.*, "On the Second-Harmonic Null in Design Space of Power Amplifiers," *IEEE Microw. Wirel. Compon. Lett.*, pp. 1–3, 2018.

[14] P. Colantonio, F. Giannini, G. Leuzzi, and E. Limiti, "High efficiency low-voltage power amplifier design by second-harmonic manipulation," *Int. J. RF Microw. Comput.-Aided Eng.*, vol. 10, no. 1, pp. 19–32, Dec. 1999.

[15] T. Sharma *et al.*, "High-Efficiency Input and Output Harmonically Engineered Power Amplifiers," *IEEE Trans. Microw. Theory Tech.*, vol. PP, no. 99, pp. 1–13, 2017.

[16] P. M. White, "Effect of input harmonic terminations on high efficiency class-B and class-F operation of PHEMT devices," in *1998 IEEE MTT-S International Microwave Symposium Digest (Cat. No.98CH36192)*, 1998, vol. 3, pp. 1611–1614 vol.3.

[17] T. Canning, P. Tasker, and S. Cripps, "Waveform Evidence of Gate Harmonic Short Circuit Benefits for High Efficiency X-Band Power Amplifiers," *IEEE Microw. Wirel. Compon. Lett.*, vol. 23, no. 8, pp. 439–441, Aug. 2013.

[18] S. K. Dhar, T. Sharma, N. Zhu, D. Holmes, R. Darraji, and F. M. Ghannouchi, "Comprehensive Analysis of Input Waveform Shaping for Efficiency Enhancement in Class B Power Amplifiers," in *2019 IEEE MTT-S International Microwave Symposium (IMS)*, 2019, pp. 1164–1167.

[19] A. Alizadeh and A. Medi, "Investigation of a Class-J Mode Power Amplifier in Presence of a Second-Harmonic Voltage at the Gate Node of the Transistor," *Ieee Trans. Microw. Theory Tech.*, vol. 65, no. 8, pp. 3024–3033, Aug. 2017.

[20] M. Haynes, S. C. Cripps, J. Benedikt, and P. J. Tasker, "PAE improvement using 2nd harmonic source injection at x-band," in *2012 Workshop on Integrated Nonlinear Microwave and Millimetre-wave Circuits*, 2012, pp. 1–3.

[21] S. K. Dhar *et al.*, "Investigation of Input–Output Waveform Engineered Continuous Inverse Class F Power Amplifiers," *IEEE Trans. Microw. Theory Tech.*, vol. 67, no. 9, pp. 3547–3561, Sep. 2019.

[22] G. Bosi, A. Raffo, G. Vannini, E. Cipriani, P. Colantonio, and F. Giannini, "Gate waveform effects on high-efficiency PA design: An experimental validation," in *2014 9th European Microwave Integrated Circuit Conference*, 2014, pp. 329–332.

[23] S. K. Dhar *et al.*, "Input-Harmonic-Controlled Broadband Continuous Class-F Power Amplifiers for Sub-6-GHz 5G Applications," *IEEE Trans. Microw. Theory Tech.*, pp. 1–14, 2020.
[24] J. Milton. Miller, "Dependence of the input impedance of a three-electrode vacuum tube upon the load in the plate circuit," U.S. Dept. of Commerce, Bureau of Standards : U.S. Govt. Print. Off., Washington, D.C., 1919.
[25] "Focus Device Characterization Suite (FDCS)." [Online]. Available: https://focus-microwaves.com/fdcs/.
[26] N. Zhu, R. McLaren, J. S. Roberts, D. G. Holmes, M. Masood, and J. K. Jones, "Compact High-Efficiency High-Power Wideband GaN Amplifier Supporting 395 MHz Instantaneous Bandwidth," in *2019 IEEE MTT-S International Microwave Symposium (IMS)*, 2019, pp. 1175–1178.
[27] A. Maekawa, T. Yamamoto, E. Mitani, and S. Sano, "A 500W Push-Pull AlGaN/GaN HEMT Amplifier for L-Band High Power Application," in *2006 IEEE MTT-S International Microwave Symposium Digest*, 2006, pp. 722–725.
[28] T. Sugitani, K. Iyomasa, M. Hangai, Y. Kawamura, J. Nishihara, and S. Shinjo, "2.45 GHz ISM-Band 450W High Efficiency GaN Pallet Amplifier for Microwave Heating," in *2018 Asia-Pacific Microwave Conference (APMC)*, 2018, pp. 1621–1623.
[29] H. Liu and Y. Jiang, "UHF-Band 4kW Broadband High Efficiency GaN Amplifier," in *2018 International Conference on Microwave and Millimeter Wave Technology (ICMMT)*, 2018, pp. 1–3.
[30] I. Takenaka *et al.*, "High-Efficiency and High-Power Microwave Amplifier Using GaN-on-Si FET With Improved High-Temperature Operation Characteristics," *IEEE Trans. Microw. Theory Tech.*, vol. 62, no. 3, pp. 502–512, Mar. 2014.
[31] H. Jang and R. Wilson, "A 225 Watt, 1.8-2.7 GHz Broadband Doherty Power Amplifier with Zero-Phase Shift Peaking Amplifier," in *2018 IEEE/MTT-S International Microwave Symposium - IMS*, 2018, pp. 797–800.
[32] Jingchu He, Tao Zhang, Yong Zhang, Yinan Wang, Binghui Zhang, and J. Gajadharsing, "A 500-W high efficiency LDMOS classical three-way Doherty amplifier for base-station applications," in *2016 IEEE MTT-S International Microwave Symposium (IMS)*, 2016, pp. 1–4.
[33] Lei Zhao, G. Bigny, and J. Jones, "A 120 watt, two-stage, LDMOS power amplifier IC at 1.8 GHz for GSM/EDGE applications," in *2008 IEEE MTT-S International Microwave Symposium Digest*, 2008, pp. 1509–1512.
[34] Younkyu Chung, Jinseong Jeong, Yuanxun Wang, D. Ahn, and T. Itoh, "Power level-dependent dual-operating mode LDMOS power amplifier for CDMA wireless base-station applications," *IEEE Trans. Microw. Theory Tech.*, vol. 53, no. 2, pp. 739–746, Feb. 2005.
[35] Younkyu Chung, Yuanxun Wang, D. Ahn, and T. Itoh, "Efficiency-enhancing technique: LDMOS power amplifier using dual-mode operation design approach," in *2004 IEEE MTT-S International Microwave Symposium Digest (IEEE Cat. No.04CH37535)*, 2004, vol. 2, pp. 859-862 Vol.2.
[36] J. Estes *et al.*, "An internally matched LTCC 3G W-CDMA 180 watt LDMOS power amplifier," in *2001 IEEE MTT-S International Microwave Sympsoium Digest (Cat. No.01CH37157)*, 2001, vol. 2, pp. 1357–1358 vol.2.
[37] Y. Park, J. Lee, S. Jee, S. Kim, and B. Kim, "Gate Bias Adaptation of Doherty Power Amplifier for High Efficiency and High Power," *IEEE Microw. Wirel. Compon. Lett.*, vol. 25, no. 2, pp. 136–138, Feb. 2015.
[38] Y. Alekajbaf and N. Masoumi, "Design and Implementation of Broadband Solid State SC-Band High Power Amplifier," in *Iranian Conference on Electrical Engineering (ICEE)*, 2018, pp. 1724–1728.

Sagar K. Dhar (Student Member, IEEE) is currently pursuing his Ph.D. degree at the iRadio Lab, University of Calgary, Calgary, AB, Canada. His current research interests include high-efficiency RF power amplifiers, Doherty power amplifiers, MMIC, large signal device modeling, digital signal processing, and load–pull techniques. He has authored or co-authored over 30 refereed publications.

Mr. Dhar was a recipient of the Izaak Walton Killam Pre-Doctoral Scholarship, the AITF Doctoral Scholarship, the Open Doctoral Scholarship, the Transformative Talent Internship Award, the Academic Excellence Award, and the Research Productivity Award.

Tushar Sharma (Student Member, IEEE) received his Ph.D. degree from the University of Calgary, Alberta, Canada in 2018 with focus on the of high-efficiency gallium nitride technology characterization and design of power amplifier architectures for 5G base station applications. Thereafter, he joined as a post-doctoral research associate at the Integrated Microsystems Research Lab at Princeton University, NJ, USA, where he was involved in exploring the novel reconfigurable techniques in RF and mm-Wave transmitters (30-100 GHz) for 5G and beyond.

In 2016, he joined RF power group of NXP Semiconductors, Chandler, AZ, USA, as a research and development engineer to steer the GaN technology evaluation and pursue product development using advanced harmonic tuned classes, waveform shaping, and large-signal device modelling to support NXP's Technology and Innovations business line. His research areas include mm-wave (30–100 GHz) advanced transmitter architectures in CMOS, GaN, InP, high-power (50–300-W) broadband amplifiers for cellular infrastructure, passive/active load-pull techniques for device characterization, and waveform engineering. Dr Sharma is a recipient of the Izaak Walton Killam Pre-Doctoral Scholarship, the Alberta Science and Innovation Under 30 Future Leader Award, the Alberta Innovates Technology Future Doctoral Scholarship, the Alberta Transformative Talent Scholarship, IEEE Education Activity Board Pre Educator award, IEEE MGAYoung Professionals Achievement award and University of Calgary 2018 Early Achievement Alumni Award. He has authored or coauthored over 35 refereed publications and holds 3 US patents—awarded or pending.

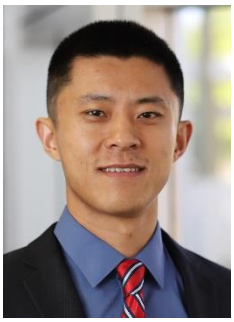

Ning Zhu (Member, IEEE) received the B.Sc. and M.Sc. degrees from the University of Electronic Science Technology of China, Chengdu, Sichuan, China, in 2006 and 2009, respectively, and the Ph.D. degree from the University of Arizona, Tucson, AZ, in 2013. Since then, he has been with Radio Power Solutions, NXP Semiconductors, Chandler, AZ, USA. He has authored and co-authored over 30 technical publications and 20 U.S. patents, awarded and pending. His research interests include high-efficiency power amplifiers, RF/mmW antennas, power harvesting, and frequency synthesis.

Ramzi Darraji (Member, IEEE) received the M.Sc. degree in communications engineering from the École Supérieure des Communications de Tunis, Ariana, Tunisia, in 2008, and the Ph.D. degree in electrical engineering from the University of Calgary, Calgary, AB, Canada, in 2013.

He is currently with Ericsson Canada Inc., Ottawa, ON, Canada. He has authored and co-authored over 50 refereed publications and holds 3 US patents. His current research interests include efficiency and bandwidth enhancement of RF power amplifiers for emerging communication systems, advanced RF front-end solutions for wireless transceivers, and digital predisortion based linearization of wireless transmitters.

Dr. Darraji was a recipient of the Natural Sciences and Engineering Research Council of Canada Post-Doctoral Fellowship, the Alberta Innovates Technology Futures Doctoral Scholarship, the IEEE Microwave Theory and Techniques Society High Achievement Award, the IEEE Wireless and Microwave Technology Conference Best Paper Award, and the Smart Radio Challenge.

Damon G. Holmes (Senior Member, IEEE) received the B.Sc. and M.Sc. degrees from the University of Calgary, Calgary, AB, Canada, in 2002 and 2005, respectively. He has gained over 15 years of industrial experience with Nortel Networks Wireless Infrastructure Group, Freescale and NXP Semiconductors, Chandler, AZ, USA, pursuing product development for transmitter architectures, advanced power amplifier design including Doherty, waveform shaping and large signal device modeling in support of cellular and wireless communication technology. He currently manages the New Technology Integration RF design efforts for cellular applications at NXP Semiconductors' Radio Power Solutions business unit. He has authored or co-authored over 20 refereed publications and has over 30 patents, awarded or pending.

Joseph Staudinger (Fellow, IEEE) is a senior technologist and Fellow at NXP Semiconductors, Chandler, Arizona. His interests are in research and product development of RF power amplifiers, transmitters, receivers, and transmitter/PA linearization for cellular and wireless networks. He is also a Faculty Associate at Arizona State University and holds more than 75 U.S. and foreign patents.

Mohamed Helaoui (Senior Member, IEEE) received the Ph.D. degree in electrical engineering from the University of Calgary, Calgary, AB, Canada, in 2008. He is currently a Professor with the Department of Electrical and Computer Engineering, University of Calgary. He has authored or coauthored over 150 publications, one book, and three book chapters, and holds 11 patent applications. His current research interests include digital signal processing, power efficiency enhancement for wireless transmitters, efficient and broadband power amplifiers, monolithic microwave-integrated circuit power amplifiers for wireless and satellite communications, six-port receivers, and advanced transceiver design for software-defined radio and millimeter-wave applications. Dr. Helaoui is also the Chair of the IEEE Local COM/MTT/AP Joint Chapter in the Southern Alberta Section.

Vince Mallette receieved his B.Sc from the University of Quebec - ETS in Montreal, Quebec, Canada in 2004. He has over 15 years of industry experience with Agilent (now Keysight), Focus Microwaves group pursuing product innovation, development and strategic business development. Currently he is the Executive Vice President of Focus Microwaves and heads all major business initiatives in terms of partnerships and growth on technology evaluation front. He has supported all different foundries ranging from silicon to III-V technologies from sub 6 GHz to mm-wave frequencies and innovation in tuner space from single frequency to harmonic tuner enabling high performance out of the device. He has authored and coauthored over 10 referred publications.

Fadhel M. Ghannouchi (Fellow, IEEE) is currently a professor, Alberta Innovates/Canada Research Chair and Director of the iRadio Laboratory in the Department of Electrical and Computer Engineering at the University of Calgary, Alberta, Canada and a part-time Thousand Talent Professor at Department of Electronics Engineering, Tsinghua University, Beijing China. His research interests are in the areas of RF and wireless communications, nonlinear modeling of microwave devices and communications systems, design of power- and spectrum-efficient microwave amplification systems and design of SDR systems for wireless, optical and satellite communications applications. He is Fellow of the Academy of Science of the Royal Society of Canada, Fellow of the Canadian Academy of Engineering, Fellow of the Engineering Institute of Canada, Fellow of the Institution of Engineering and Technology (IET) and Fellow of the Institute of Electrical and Electronic Engineering (IEEE). He published more than 800 referred papers, 6 books and hold 25 patents (3 pending). Prof. Ghannouchi is the co-founder of three university spun-off companies.